

Lattice and phonon properties in semiconductors $FeSb_2$ and $RuSb_2$

Meng Zhang(张萌), Shengnan Dai(戴胜男), Ranran Zhang(张冉冉), Mingfang Shu(舒明方), Wei Xu(徐威), Jinfeng Zhu(朱金峰), Xianglin Liu(刘祥麟), Yixuan Luo(罗伊轩), Toru Ishigaki, Bo Duan(段波), Yanfeng Guo(郭艳峰), Zhe Qu(屈哲), Jiong Yang(杨炯), and Jie Ma(马杰)

Citation: Chin. Phys. B, 2025, 34 (**8**): 086302. DOI: 10.1088/1674-1056/adda0e
http://cpb.iphy.ac.cn; http://iopscience.iop.org/cpb

What follows is a list of articles you may be interested in

Laser power-induced Fermi-level shift in graphene/Al_2O_3 under ambient atmosphere: Toward neutralizing unintentional graphene doping

Jamal Q. M. Almarashi, Mohamed K. Zayed, Hesham Fares, Heba Sukar, Takao Ono, Yasushi Kanai, and Mohamed Almokhtar

Chin. Phys. B, 2025, 34 (**6**): 066302. DOI: 10.1088/1674-1056/adc6f3

Anomalous lattice vibration in monolayer MoS_2 induced by DUV laser: A first-principles investigation

Weidong Wang(王卫东), Renhui Liu(刘仁辉), Ye Zhang(张也), Huaihong Guo(郭怀红), Jianqi Huang(黄建啟), Zhantong Liu(刘展彤), Heting Zhao(赵贺霆), Kai Wang(王凯), Bo Zhao(赵波), and Teng Yang(杨腾)

Chin. Phys. B, 2025, 34 (**6**): 066301. DOI: 10.1088/1674-1056/adc36e

Glass formation and physical properties of Sb_2S_3-CuI chalcogenide system

Qilin Ye(叶旗林), Dan Chen(陈旦), and Changgui Lin(林常规)

Chin. Phys. B, 2021, 30 (**1**): 016302. DOI: 10.1088/1674-1056/abc0e2

Raman scattering study of two-dimensional magnetic van der Waals compound VI_3

Yi-Meng Wang(王艺朦), Shang-Jie Tian(田尚杰), Cheng-He Li(李承贺), Feng Jin(金峰), Jian-Ting Ji(籍建葶), He-Chang Lei(雷和畅), Qing-Ming Zhang(张清明)

Chin. Phys. B, 2020, 29 (**5**): 056301. DOI: 10.1088/1674-1056/ab8215

Raman scattering study of magnetic layered MPS_3 crystals (M=Mn, Fe, Ni)

Yi-Meng Wang(王艺朦), Jian-Feng Zhang(张建丰), Cheng-He Li(李承贺), Xiao-Li Ma(马肖莉), Jian-Ting Ji(籍建葶), Feng Jin(金峰), He-Chang Lei(雷和畅), Kai Liu(刘凯), Wei-Lu Zhang(张玮璐), Qing-Ming Zhang(张清明)

Chin. Phys. B, 2019, 28 (**5**): 056301. DOI: 10.1088/1674-1056/28/5/056301

RAPID COMMUNICATION

Lattice and phonon properties in semiconductors $FeSb_2$ and $RuSb_2$

Meng Zhang(张萌)[1], Shengnan Dai(戴胜男)[2,†], Ranran Zhang(张冉冉)[3], Mingfang Shu(舒明方)[1], Wei Xu(徐威)[1], Jinfeng Zhu(朱金峰)[1], Xianglin Liu(刘祥麟)[4], Yixuan Luo(罗伊轩)[4], Toru Ishigaki[5], Bo Duan(段波)[6], Yanfeng Guo(郭艳峰)[4,7], Zhe Qu(屈哲)[3], Jiong Yang(杨炯)[2], and Jie Ma(马杰)[1,‡]

[1] *Key Laboratory of Artificial Structures and Quantum Control, School of Physics and Astronomy, Shanghai Jiao Tong University, Shanghai* 200240, *China*
[2] *Materials Genome Institute, Shanghai University, Shanghai* 200444, *China*
[3] *Anhui Key Laboratory of Low-Energy Quantum Materials and Devices, High Magnetic Field Laboratory, Hefei Institutes of Physical Science, Chinese Academy of Sciences, Hefei* 230031, *China*
[4] *School of Physical Science and Technology, ShanghaiTech University, Shanghai* 201210, *China*
[5] *Neutron Industrial Application Promotion Center, Comprehensive Research Organization for Science and Society, Naka, Ibaraki* 319-1106, *Japan*
[6] *Hubei Key Laboratory of Theory and Application of Advanced Materials Mechanics, School of Science, Wuhan University of Technology, Wuhan* 430070, *China*
[7] *ShanghaiTech Laboratory for Topological Physics, ShanghaiTech University, Shanghai* 201210, *China*

(Received 5 April 2025; revised manuscript received 6 May 2025; accepted manuscript online 19 May 2025)

The family of transition-metal dipnictides, MX_2 (M: metal, X: N, P, As, Sb, and Bi), has emerged as an important quantum material system due to its unique physical properties, such as large magnetoresistance, colossal Seebeck coefficients, and Weyl semimetal characteristics. In order to study the M-site ions effect on the lattice structure and the related dynamics, we compared two isostructural compounds, $FeSb_2$ and $RuSb_2$. Neutron diffraction, specific heat, and Raman scattering spectra of $RuSb_2$ were measured. We found that the thermal expansion coefficients are isotropic for $RuSb_2$, in contrast to the anisotropic behavior reported previously in $FeSb_2$. Moreover, the specific heat of $RuSb_2$ shows a boson-like anomaly around 25 K. Four of the six predicted vibrational modes were identified by polarized Raman scattering spectra and successfully simulated by *ab initio* calculations. Meanwhile, the temperature-dependent linewidths reveal that phonon–phonon interactions might dominate above 50 K, while electron–phonon coupling remains relatively weak.

Keywords: transition-metal dipnictide, neutron diffraction, Raman, boson-like peak

PACS: 63.20.–e, 61.05.F–, 63.20.Ry, 78.30.–j

DOI: 10.1088/1674-1056/adda0e **CSTR:** 32038.14.CPB.adda0e

1. Introduction

Transition-metal dipnictides of the MX_2 family, where M represents the transition metal and X denotes the phosphorus group, have become one of the important research frontiers owing to their exotic physical properties and the related states. For example, WP_2 and MoP_2 show extremely high electrical conductivity and large magnetoresistance (MR) from the spin texture induced by Weyl points.[1–5] In contrast, $NbAs_2$ and $TaAs_2$ exhibit resistivity plateau and large MR at low temperatures and high fields due to the field-induced metal–insulator transition or Kohler's rule.[6–8] Among them, MSb_2 (M = Fe, Ru, Cr) have garnered significant attention due to their promising thermoelectric (TE) properties.[9–12] For instance, $FeSb_2$ presents a colossal Seebeck coefficient (S) and a record-large TE power factor, attributed to the phonon-drag effect.[9] To investigate the ionic effect on these properties, the isostructural compound $RuSb_2$ has also been studied, revealing a conventional band semiconductor behavior (or slight electron correlation) with an energy gap of 0.19 eV.[13] Meanwhile, its magnetic susceptibility (χ) displays nearly temperature-independent diamagnetism,[12] and a high positive MR was observed at 2 K in the *ab* plane of $RuSb_2$.[14] The static and dynamic information of materials is key for understanding and regulating their mechanical, thermodynamic, and electronic properties. While previous studies have focused on electronic contributions to these properties, the thermal effect and the related lattice dynamics of $RuSb_2$ remain unexplored.

Hence, we carried out structural and thermodynamic studies to further elucidate the difference in the structure and thermal properties of $RuSb_2$ and $FeSb_{1.8}$. Temperature-dependent neutron diffraction measurements were performed to track the evolution of the lattice parameters in both compounds. Furthermore, the specific heat of $RuSb_2$ exhibited a boson-like peak around 25 K, and the phonon behaviors of $RuSb_2$ were captured by the Raman experiment and simulated by density functional theory (DFT) calculations. By delving into the intricacies of lattice and phonon dynamics, a method of developing advanced materials with optimized functionali-

†Corresponding author. E-mail: musenc@shu.edu.cn
‡Corresponding author. E-mail: jma3@sjtu.edu.cn

© 2025 Chinese Physical Society and IOP Publishing Ltd. All rights, including for text and data mining, AI training, and similar technologies, are reserved.

ties was suggested.

2. Results and discussion

2.1. Synthesis

$RuSb_2$ crystals were grown using the self-flux method. Starting materials of high-purity Ru powder (99.9%) and Sb granules (99.999%) were mixed in a molar ratio of 1:10 and placed into an alumina crucible. The crucible was sealed in a quartz ampoule under vacuum. The sealed quartz ampoule was heated to 1373 K within 15 hours and maintained for 20 hours, and then slowly cooled to 973 K at a rate of 1.5 K/h. The excess flux was removed using a high-speed centrifuge. Then the quartz tube was cooled to room temperature in air, leaving $RuSb_2$ single crystals with a black shiny metallic luster in the crucible.

High-purity powders of Fe (300 mesh, 99.95%) and Sb (300 mesh, 99.999%) were weighed according to the stoichiometric ratio specified by the chemical formula. The powders were thoroughly mixed using an agate mortar and pestle. The mixture was subsequently loaded into a graphite crucible which was sealed inside a quartz tube under vacuum. The quartz tube was placed in a muffle furnace and heated at a rate of 1 K/min to 903 K. The quartz tube was kept at 903 K for 72 hours and then cooled to room temperature, leaving $FeSb_{2-x}$ ($x = 0$, 0.1, 0.2) powders. Although three compositions were synthesized, only $FeSb_{1.8}$ ($x = 0.2$) presented the single phase.

2.2. Crystallographic structures

The crystal structures of $RuSb_2$ and $FeSb_{1.8}$ at 300 K were measured by neutron powder diffraction (NPD). The Rietveld analysis confirmed that both compounds crystallized in the orthorhombic space group *Pnnm* (No. 58) without discernible impurities, as shown in Figs. 1(a) and 1(b). Consistent with previous report, the derived lattice parameters are $a = 5.953425(11)$ Å, $b = 6.675597(12)$ Å, $c = 3.181239(5)$ Å for $RuSb_2$ and $a = 5.832623(3)$ Å, $b = 6.538084(3)$ Å, $c = 3.197367(2)$ Å for $FeSb_{1.8}$.[15] The smaller lattice parameter ratios of $RuSb_2$ ($c/a \sim 0.53$ and $c/b \sim 0.47$) compared to those of $FeSb_{1.8}$ ($c/a \sim 0.54$ and $c/b \sim 0.48$), as well as the Ru–Sb–Ru angle (φ) less than 90°, lead to the formation of the regular marcasite structure. The crystal structures of $RuSb_2$ and $FeSb_{1.8}$ are represented in the inset of Fig. 1(b), where the Ru (Fe) ions are surrounded by distorted Sb octahedra, and the structural units, $RuSb_6$ ($FeSb_6$) octahedra, share edges along the *c*-axis. Furthermore, to validate the experimental lattice parameters, first-principles calculations were performed by employing the advanced r^{2}SCAN functional. The optimized lattice constants for $RuSb_2$ are $a = 5.9786$ Å, $b = 6.7051$ Å, and $c = 3.2162$ Å.

To explore the thermal expansion process in $RuSb_2$ and $FeSb_{1.8}$, the temperature-variable NPD measurements were performed. The crystallographic structures of $RuSb_2$ and $FeSb_{1.8}$ can be well fitted using the same structural model

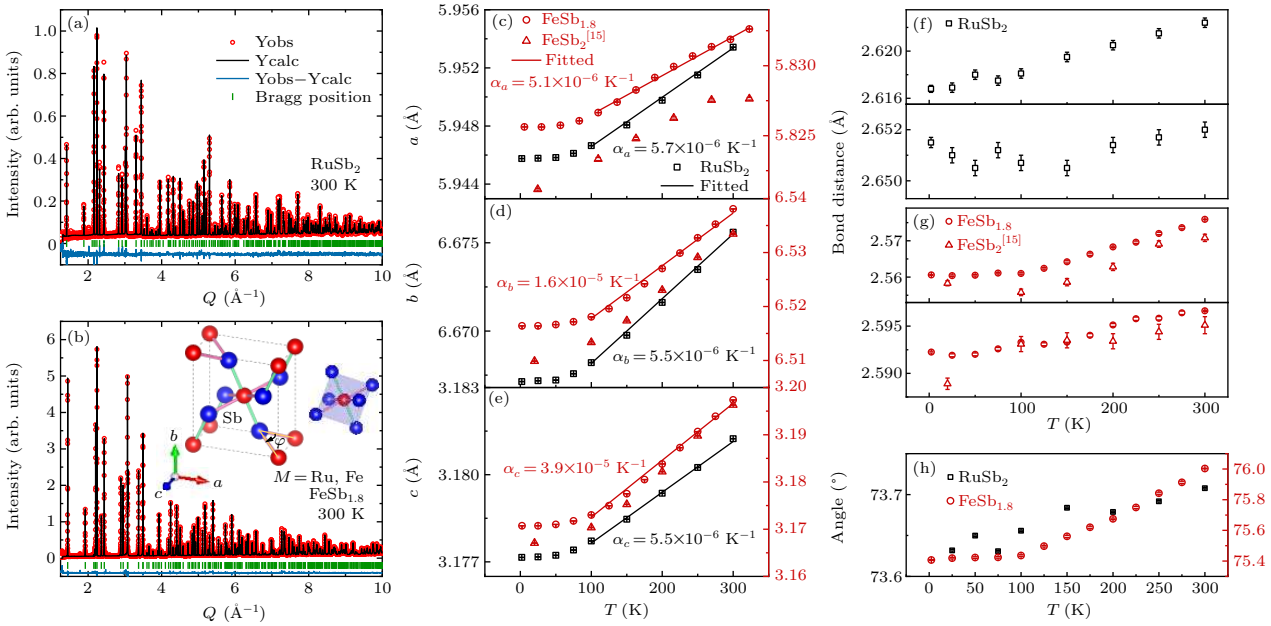


Fig. 1. Rietveld refinement of neutron diffraction data measured at 300 K for (a) $RuSb_2$ and (b) $FeSb_{1.8}$. The green vertical bars indicate the expected Bragg reflection positions and the bottom blue curves show the difference between the observed and calculated patterns. The inset of (b): crystal structure of XSb_2 (X: Ru, Fe) showing X (red) surrounded by Sb (blue) octahedra. The angle φ of X–Sb–X is constructed by two yellow solid lines. The shorter and longer X–Sb bonds are shown in green and pink solid lines, respectively. The single unit cell is plotted using dashed lines. (c)–(e) Lattice parameters as a function of temperature from 2 K to 300 K in $RuSb_2$, $FeSb_{1.8}$, and $FeSb_2$.[15] The solid line denotes the fitting of the linear thermal expansion coefficients. Temperature dependence of (f), (g) X–Sb bond lengths, and (h) X–Sb–X angles from 2 K to 300 K for $RuSb_2$ and $FeSb_{1.8}$. The top panels of (f) and (g) show the temperature dependence of the shorter X–Sb bonds, while the bottom panels of (f) and (g) illustrate the temperature dependence of the longer X–Sb bonds.

throughout the temperature range of 2–300 K, suggesting the absence of any phase transitions. Figures 1(c)–1(e) present the temperature dependence of the lattice parameters a, b, and c for $RuSb_2$, $FeSb_{1.8}$, and $FeSb_2$[15] from 2 K to 300 K. The lattice parameters for $RuSb_2$ are temperature-independent at $T < 50$ K and then increase linearly with the temperature above 50 K. The linear thermal expansion coefficients $\alpha_i = 1/l\ (\partial l/\partial T)$ $(i = a,\ b,\ c)$ can be extracted from the lattice constants data fitted above 100 K. The thermal expansion coefficients of $RuSb_2$ are nearly isotropic with $\alpha_a = 5.7(2) \times 10^{-6}$ K^{-1} and $\alpha_{b,c} = 5.5(2) \times 10^{-6}$ K^{-1}. In contrast, $FeSb_{1.8}$ shows anisotropic thermal expansion characteristics, demonstrating distinct values along different crystallographic axes: $\alpha_a = 5.1(0) \times 10^{-6}$ K^{-1}, $\alpha_b = 1.6(0) \times 10^{-5}$ K^{-1}, and $\alpha_c = 3.9(1) \times 10^{-5}$ K^{-1}. Although the Sb vacancy concentrations differ between $FeSb_{1.8}$ and $FeSb_2$, the overall trends in the temperature dependence of the lattice parameters are similar. For comparison, the linear thermal expansion coefficients of $FeSb_2$ are $\alpha_a = 4.2 \times 10^{-6}$ K^{-1}, $\alpha_b = 1.3 \times 10^{-5}$ K^{-1}, and $\alpha_c = 3.4 \times 10^{-5}$ K^{-1}.[15]

The linear thermal expansion of lattice constants correlates with bond length elongation and bond angle variations. As shown in Figs. 1(f) and 1(g), above 100 K, the shorter Fe–Sb bonds undergo accelerated thermal expansion compared to the Ru–Sb counterparts. Meanwhile, the bond angles φ in $FeSb_{1.8}$ demonstrate remarkably stronger temperature-dependent variations than those in $RuSb_2$ (Fig. 1(h)). These coordinated structural responses collectively contribute to the pronounced anisotropic lattice expansion along the b- and c-axes in $FeSb_{1.8}$, different from those observed in $RuSb_2$.

2.3. Specific heat

To gain insights into the lattice dynamics and anharmonic effects in $RuSb_2$, we systematically investigated its specific heat behavior. The specific heat, C_P, can be well fitted by the Debye–Einstein model[16]

$$C_P = \beta T + 9R\frac{\sum_i A_i}{(n-1)}\left(\frac{T}{\Theta_D}\right)^3 \int_0^{\frac{\Theta_D}{T}} \frac{\varepsilon^4 e^{\varepsilon}}{(e^{\varepsilon}-1)^2} d\varepsilon + 3R\sum_i A_i \frac{\left(\frac{\Theta_{Ei}}{T}\right)^2 e^{\frac{\Theta_{Ei}}{T}}}{\left(e^{\frac{\Theta_{Ei}}{T}}-1\right)^2}, \quad \varepsilon = \frac{\Theta}{T}, \tag{1}$$

where β represents the electronic contribution to the specific heat, and the small value can be neglected. R is the gas constant, and n is the number of atoms in a unit cell. As shown in Fig. 2(a), using Debye temperature $\Theta_D = 219$ K and Einstein temperatures $\Theta_{E1} = 130$ K and $\Theta_{E2} = 291$ K, the calculated C_P agrees well with our experimental data. The C_P/T^3 vs. T plot, as shown in Fig. 2(b), reveals a boson-like peak around 25 K, which is a signature typically associated with glassy systems.[17,18]

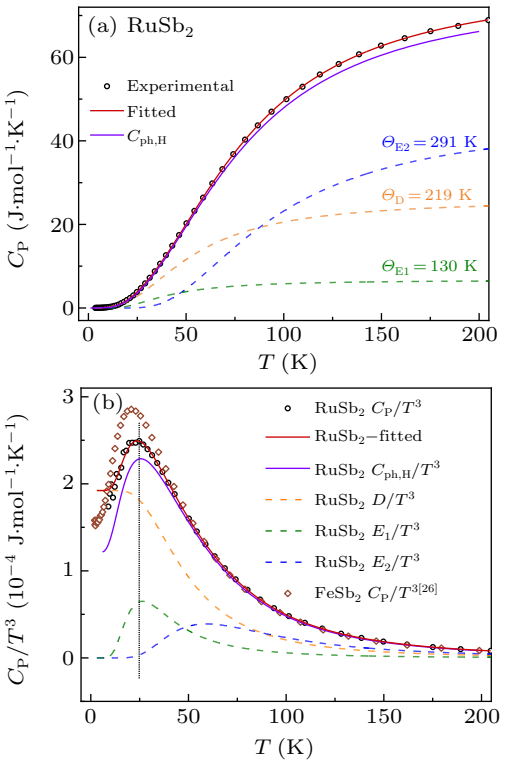


Fig. 2. (a) Heat capacities, C_P, of $RuSb_2$ fitted with one Debye and two Einstein modes. The black circles are experimental values measured by PPMS. Calculated heat specific from harmonic phonons, $C_{ph,H}$, is shown in purple solid line. The contributions of Debye and two Einstein modes are denoted in orange dotted, blue dashed, and green dashed lines, respectively. (b) C_P/T^3 vs. T plot shows a hump peak for $RuSb_2$ and $FeSb_2$,[26] demonstrating the necessity of the combined Debye–Einstein model in the fitting.

To probe the origin of this anomaly, we perform another method to analyze the specific heat quantitatively based on the calculated phonon density-of-states (DOS), $g(E)$. $C_{ph,H}$ is the harmonic phonon contributions from the $g(E)$ by the DFT calculations[19,20]

$$C_{ph,H} = T\,dS_{ph}/dT, \tag{2}$$

$$S_{ph} = 3k_B \int dE\, g(E)\,[(n+1)\ln(n+1) - n\ln n], \tag{3}$$

where $n = \frac{1}{\exp[E/(k_B T)]-1}$.

As temperature increases, the $C_{ph,H}$ gradually deviates from the experimental data, signaling the emergence of significant anharmonic effects. The thermal properties of these crystalline materials are different from positional disorder[21,22] observed in glasses, but are associated with phonon softening or strong phonon–phonon interactions, often driven by enhanced anharmonicity,[23–25] which are observed in molecular crystals,[24] zintl-type Sr(Cu,Ag,Zn)Sb[16] and InSe,[20] etc. Key thermodynamic parameters extracted from specific heat measurements show the Einstein temperature, Θ_{E1} =

130 K, of $RuSb_2$ lies substantially below its Debye temperature $\Theta_D = 219$ K. Crucially, the boson-like peak position matches with the characteristic E_1/T^3 crossover near 25 K for $RuSb_2$, strongly suggesting the existence of acoustic-optical phonon interactions. A comparative analysis also reveals the boson-like peak in $FeSb_2$ but it occurs at a lower temperature (~ 20 K) and will be discussed with the Raman data later.

2.4. Raman spectroscopy

To analyze the phonon properties, we performed Raman spectroscopy experiments and DFT calculations. After calibrating using normative Si film, we measured the Raman spectra by unpolarized detection. Figure 3(a) depicts the Raman spectrum for the single crystal $RuSb_2$ from 5 K to 300 K. Four Raman-active vibrational modes can be identified with shifts ranging between 170 cm^{-1} and 220 cm^{-1}, and there is no structural phase transition. The Raman modes were numbered as I to IV from lowest to highest wavenumber, 177.0 cm^{-1}, 186.7 cm^{-1}, 201.3 cm^{-1}, and 219.8 cm^{-1} at 5 K, respectively. While the intensity of mode I exhibits only moderate temperature dependence, the intensities of modes II, III, and IV display substantial changes with increasing temperature. It is worth noting that mode III is weak and vanishes around 275 K in some orientation. All the Raman peaks redshift and broaden as the temperature rises.

The angle dependence of the polarized Raman spectrum was applied to investigate the vibration modes. Factor-group analysis shows all optical vibration modes at the Brillouin zone center as $\Gamma = 2A_g + 2B_{1g} + B_{2g} + B_{3g} + 2A_u + 2B_{1u} + 4B_{2u} + 4B_{3u}$ with 6 Raman (R) active and 12 infrared (IR) active modes. Among them, $2A_g$, $2B_{1g}$, B_{2g}, and B_{3g} modes are R active and the Raman tensors are

$$\chi(A_g) = \begin{pmatrix} a & 0 & 0 \\ 0 & b & 0 \\ 0 & 0 & c \end{pmatrix}, \quad \chi(B_{1g}) = \begin{pmatrix} 0 & d & 0 \\ d & 0 & 0 \\ 0 & 0 & d \end{pmatrix},$$
$$\chi(B_{2g}) = \begin{pmatrix} 0 & 0 & e \\ 0 & 0 & 0 \\ e & 0 & 0 \end{pmatrix}, \quad \chi(B_{3g}) = \begin{pmatrix} 0 & 0 & 0 \\ 0 & 0 & f \\ 0 & f & 0 \end{pmatrix}, \tag{4}$$

where a, b, c, d, e, and f represent the values of the tensor elements. The Raman intensity is given quantitatively by

$$I \propto |\langle \hat{e}_i | \chi | \hat{e}_s \rangle|^2, \tag{5}$$

where $\hat{e}_i$ and $\hat{e}_s$ are the unit vectors of the polarized incident and scattered light, respectively. The crystallographic orientation dependence is defined by the rotation angle θ between the a-axis of the sample and the incident light propagation vector, as shown in Fig. 3(b). For the polarized Raman configuration: $\hat{e}_i = \hat{e}_s = (\cos\theta, \sin\theta, 0)$ with parallel polarization, $\hat{e}_i = (\cos\theta, \sin\theta, 0)$ and $\hat{e}_s = (-\sin\theta, \cos\theta, 0)$ with cross-polarization. Under different polarization configurations, the angle dependence will be different and the periodical Raman intensity is shown in Table 1. Only A_g and B_{1g} modes are visible in the spectra when the incident light lies within the ab plane, while B_{2g} and B_{3g} modes are forbidden.

Table 1. The angle dependence of Raman mode intensities with rotating crystals in the parallel and cross-polarization configurations are given.

	A_g	B_{1g}	B_{2g}	B_{3g}
Parallel	$(a\cos^2\theta + b\sin^2\theta)^2$	$d^2\sin^2 2\theta$	0	0
Cross	$0.25(b-a)^2\sin^2 2\theta$	$d^2\cos^2 2\theta$	0	0

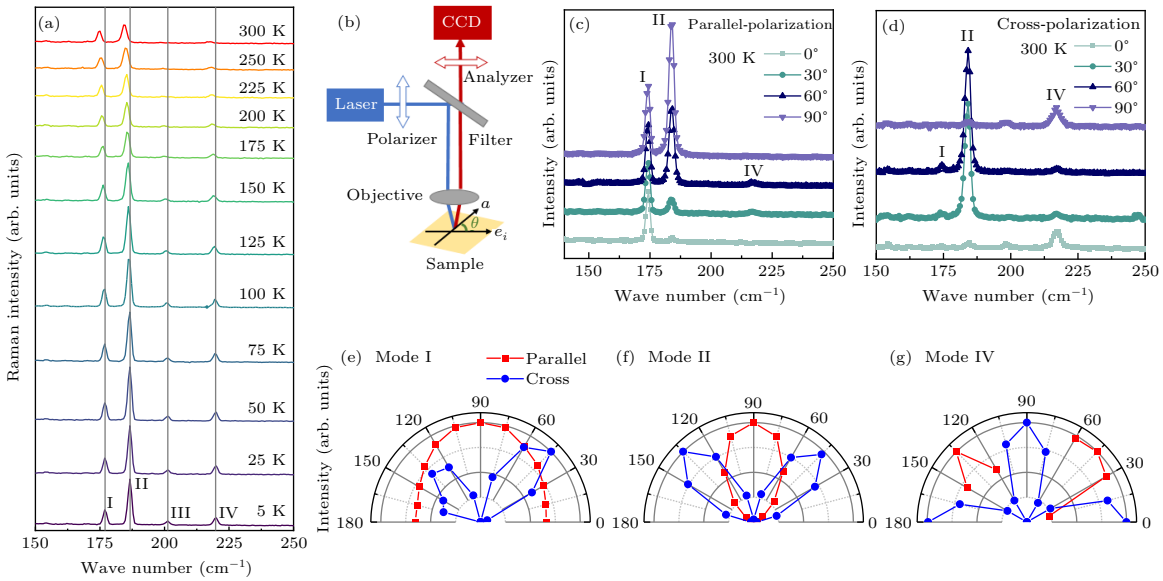


Fig. 3. (a) Unpolarized Raman spectra as a function of temperature for $RuSb_2$. (b) Schematic diagram of polarized Raman spectroscopy. Raman spectra of $RuSb_2$ with different sample rotation angles θ at 300 K under (c) the parallel and (d) the cross-polarization configurations. Polar plots of the fitted peak intensities of (e) I, (f) II, and (g) IV modes as a function of rotation angle θ under the parallel and the cross-polarization configurations.

The angle-dependent Raman measurements at 300 K were performed to determine the symmetries of the observed Raman modes. Figures 3(c) and 3(d) show the polarized Raman spectra at different rotation angles $\theta = 0°$, 30°, 60°, and 90° under both parallel and cross-polarization configurations. The mode III was barely detectable at 300 K due to the weak intensity. The intensities of modes I, II, and IV exhibit angular dependence. The intensities of mode IV are relatively weak under the parallel configuration, while the intensities of mode I are comparatively reduced under the cross-polarization configuration.

To further confirm the observation of the angle-resolved polarized Raman intensity, the Raman spectra of $RuSb_2$ single crystal were measured in both parallel and cross-polarization configurations as the sample rotated from 0° to 180°. Figures 3(e)–3(g) present the normalized polar plots of the fitted peak intensities of these Raman modes as a function of the sample rotation angle θ, excluding the mode III with low intensity. For the parallel configuration, the intensities of modes I and II present two-fold symmetry. Specifically, their intensities reach a maximum at $\theta = 90°$and a minimum at $\theta = 0°$ or 180°. The intensity of the IV Raman mode exhibits a four-fold periodicity with a period of 90°, reaching the maximum at $\theta = 45°/135°$. On the other hand, in the cross-configuration, the modes I and II show a four-fold period of 90° with maximum intensities observed at $\theta = 45°$ and 135°. It can be clearly seen that the intensities of modes I and II are proportional to $\sin^2 2\theta$, indicating that they belong to A_g modes. The intensity of mode IV reaches its maximum at $\theta = 0°$ or 90° and is forbidden at $\theta = 45°$ or 135°, hence, the mode III is B_{1g} mode. Furthermore, by elimination, mode III should be the B_{1g} mode.

Several factors can contribute to changing the linewidth, such as structural disorders, isotopic effects, anharmonic effects, electron–phonon interactions, etc.,[27] however, only anharmonic effects and electron–phonon interactions are likely to introduce temperature dependence. Figure 4 illustrates the temperature dependence of the energy and linewidth for those four modes. Below 50 K, the linewidth and energy of Raman peaks remain nearly constant; while above 50 K, both quantities exhibit significant variation with increasing temperature. Furthermore, the lattice constants remain constant until 50 K, as shown in Fig. 1. Taking the anharmonic effects based on three-phonon processes into account,[27–29] the experimental data of FWHM and wave number are respectively fitted by

$$\Gamma(T) = \Gamma_0 + A\left(1 + \frac{2}{e^x - 1}\right), \tag{6}$$

$$\omega(T) = \omega_0 - C\left(1 + \frac{2}{e^x - 1}\right), \tag{7}$$

where Γ_0 includes intrinsic linewidth, structural disorder, isotopic effect, and temperature-independent electron–phonon interaction contribution, A is the anharmonic constant, $x = \hbar\omega_0/(2k_BT)$, ω_0 is temperature-independent contributions, and C is the anharmonic constant.

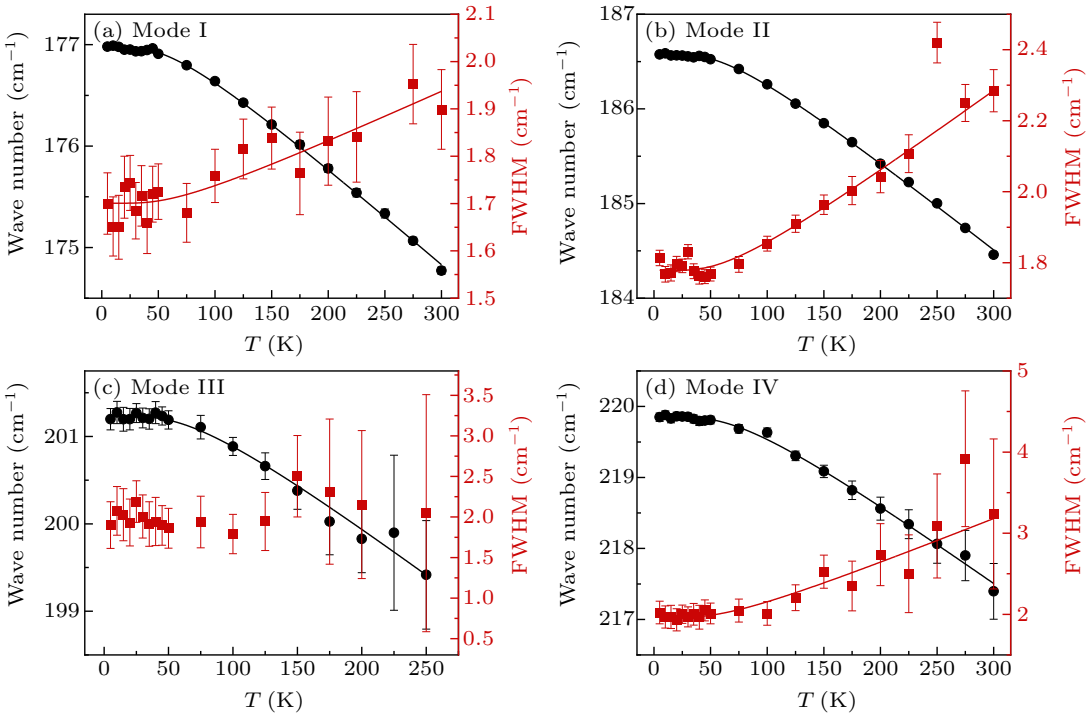


Fig. 4. Temperature-dependence of the wave numbers and FWHMs of modes (a) I, (b) II, (c) III, and (d) IV in $RuSb_2$.

The phonon frequencies of the four modes fit well with Eq. (7), which suggests that the phonon–phonon interactions become more pronounced with increasing temperature, accompanied by mode softening. Similar behavior, characterized by narrower linewidths of A_g modes and weaker electron–phonon coupling constants, has been discussed in Ta(Nb)As_2, which was induced by small electron–phonon coupling.[30] For $FeSb_2$, the anomalies were explained by a change in the electron–phonon interaction.[31,32] At zero temperature, phonon–phonon scattering is negligible due to phonon freezing, and the phonon linewidths at this temperature are primarily attributed to impurities and electron–phonon interactions.[30] As the symmetric line shapes and the linewidths at low temperatures are smaller than those of $FeSb_2$,[27] $RuSb_2$ should not include strong electron–phonon coupling. The stronger localization and electron correlation effects associated with 3d electrons make $FeSb_2$ more prone to exhibiting significant electron–phonon coupling compared to $RuSb_2$ with 4d electrons. In conclusion, for $RuSb_2$, the temperature dependence of linewidth increases mainly due to the phonon–phonon interactions, and the electron–phonon coupling is weak.

The phonon lifetime, τ, can be calculated using $\tau_i = 1/(2\pi \mathrm{FWHM}_i)$,[33] and the results are presented in Fig. 5. The phonon lifetimes of $RuSb_2$ are distributed within the range of 4–9 ps at temperatures between 5 K and 300 K, comparable to those reported for $FeSb_2$,[27] a material known for its relatively high thermal conductivity. As the temperature increases, anharmonic effects cause the calculated τ to decrease, thereby leading to the reduction of thermal conductivity.[9]

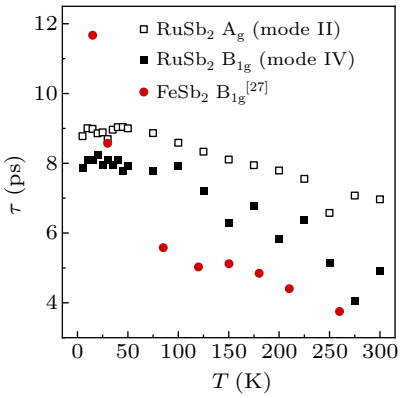


Fig. 5. The lifetime, τ, of the Raman modes for $RuSb_2$ and $FeSb_2$[27] as a function of temperature.

2.5. *Ab initio* calculations

In order to determine the vibrating modes between the ions, both acoustic and optical phonons were calculated. Figure 6(a) shows that the energy of soft optical phonons is comparable to that of the top acoustic phonons. The interaction between the acoustic phonons and optical phonons is likely responsible for the boson-like peak observed in $RuSb_2$. Compared to $RuSb_2$, the lower position of the boson-like peak in $FeSb_2$ may be attributed to the lower energy crossing (interaction) between acoustic and optical phonons. The maximum energy of the acoustic phonons along the Γ–Z direction is around 150 cm^{-1}, corresponding to $\Theta_D = 219$ K extracted from the measured specific heat.

The phonon DOS of $RuSb_2$ and $FeSb_2$[34] are represented in Fig. 6(b). Due to the heavier atomic mass of Ru compared to Fe, the high-energy optical branches of $RuSb_2$ soften. In contrast, the acoustic and mid-energy optical branches are hardened, resulting in stronger hybridization between the non-localized Ru 4d orbitals and the Sb orbitals.[35]

Raman modes were analyzed based on DFT calculations. The atomic vibration patterns and frequencies of Raman active modes are shown in Fig. 6(c). Due to the *Pnnm* space group with the Ru atom located at the center of inversion, the vibrations involving Ru atoms are Raman inactive; and Raman active modes originate only from the Sb atom vibrations. Among Raman active modes, the B_{2g} and B_{3g} modes exhibit vibrational motions along the *c*-axis, whereas the A_g and B_{1g} modes are characterized by vibrations within the *ab*-plane. Modes I and II are both A_g modes; mode I primarily vibrates along the *a*-axis, while mode II dominates the vibration along the *b*-axis. As shown in Fig. 4, mode II exhibits a more significant change in FWHM than mode I. This difference is likely induced by the distinct vibrational characteristics of each mode. The calculated Raman frequencies are in good agreement with experimental measurements.

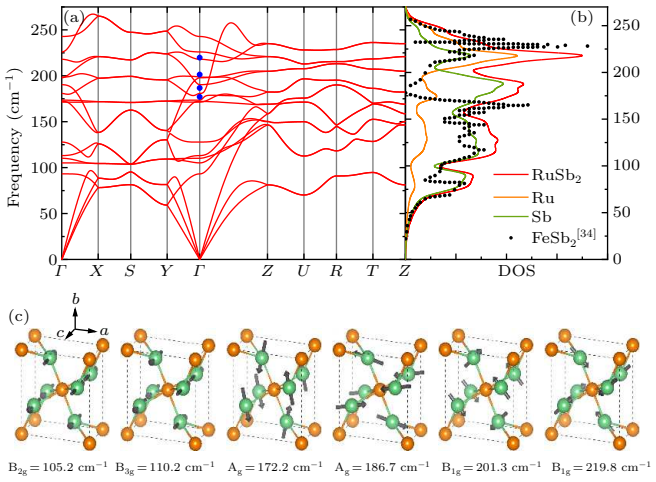


Fig. 6. (a) Phonon dispersions for $RuSb_2$, (b) DOSs for $RuSb_2$ and $FeSb_2$.[34] (c) Schematic of the eigenvectors for the Raman active modes in $RuSb_2$. Blue circles in panel (a) represent experimentally observed Raman mode energies at 5 K.

3. Experimental details

3.1. Neutron diffraction experiments

The variable temperature neutron powder diffraction (NPD) data were performed on the time-of-flight (TOF) neu-

tron diffractometer iMATERIA located at the Materials and Life Science Experimental Facility, J-PARC, Tokai, Ibaraki, Japan. A closed-cycle He-refrigerator was used to control the sample environment over the temperature range of ~ 2 K to 300 K. The NPD data were refined by the Rietveld method with the program Z-Rietveld.

3.2. Raman experiments

The Raman scattering measurements were recorded in the backscattering geometry with a 532-nm laser as an excitation source (HORIBA J.Y.T64000) at High Magnetic Field Laboratory (Hefei, China). Low temperature was maintained by a closed-cycle He-cryostat (ST500) attached to the spectrometer. A sample rotation stage was used to change the orientation of the sample. All Raman measurements were performed on this flat surface, which was determined to be *ab* plane by Laue diffraction.

3.3. Specific heat measurement

The temperature dependence of specific heat was obtained using a commercial physical property measurement system (PPMS) with zero magnetic fields.

3.4. First-principles calculations

The *ab initio* calculations were performed in the framework of density functional theory, as implemented in the Vienna *ab initio* simulation package (VASP),[37,38] using the projector-augmented wave[39] method. The r^{2}SCAN meta-GGA functional[40] was selected for its improved numerical performance, and a plane-wave energy cutoff of 520 eV was adopted. For the structural optimization, the k-point mesh was chosen as $11 \times 11 \times 17$. Phonon dispersion and related physical quantities were calculated using the frozen phonon method, implemented in the Phonopy code.[41,42] The $3 \times 3 \times 6$ supercells with displacements were used in this procedure, with an energy convergence criterion of 10^{-7} eV and a force convergence accuracy of 10^{-5} eV/Å, considering only the Γ point. Phonon vibration modes were visualized through the TSS Physics website.

4. Conclusion

In summary, we compared the lattice and phonon dynamics properties of the isostructural homologues $RuSb_2$ and $FeSb_2$, the latter of which has been previously reported. NPD data show that the lattice thermal expansion is isotropic for $RuSb_2$, with linear thermal expansion coefficients smaller than those of $FeSb_{1.8}$. Those differences were attributed to the more pronounced thermal expansion of the shorter Fe–Sb bond and the Fe–Sb–Fe angles in $FeSb_{1.8}$ compared to $RuSb_2$. Boson-like peaks related to the interaction between acoustic and optical phonons were observed in both $RuSb_2$ and $FeSb_2$, however, $FeSb_2$ shows a lower temperature boson peak (~ 20 K) than $RuSb_2$ (~ 25 K), which can be ascribed to a lower energy crossing between acoustic and optical phonons. Four experimentally observed Raman-active modes were identified using polarized Raman spectroscopy and confirmed by DFT calculations. In temperature-dependent Raman scattering measurements for $RuSb_2$, we observed a significant broadening of the Raman peak linewidth above 50 K, likely caused by phonon–phonon interactions. At low temperatures, the linewidth of the Raman peaks in $FeSb_2$ is relatively larger than that in $RuSb_2$, which is likely due to stronger electron–phonon interactions in $FeSb_2$. These results reveal that the difference in the boson-like peak positions between $RuSb_2$ and $FeSb_2$ originates from variations in the energy crossing between acoustic and optical phonons. This finding suggests that tuning the interaction between acoustic and optical phonons could serve as an effective approach for controlling low-temperature phonon behavior in related materials. Moreover, the spin dynamics will be measured by inelastic neutron scattering to discuss the MR effect in the transition-metal magnetic oxides.[36]

Acknowledgments

The authors thank Dr. Yu Liu and Dr. Qianheng Du for helpful discussions on the specific heat data of $FeSb_2$. Project supported by the National Natural Science Foundation of China (Grant Nos. U2032213 and 12334008), the Guangdong Provincial Key Laboratory of Extreme Conditions (Grant No. 2023B1212010002). We thank the staff members of the Micro-Raman Spectroscopy System (https://cstr.cn/31125.02.SHMFF.RAMAN) at the Steady High Magnetic Field Facility, CAS (https://cstr.cn/31125.02.SHMFF), for providing technical support and assistance in data collection and analysis. We acknowledge the beam time granted by J-PARC (proposal No. 2019A0191).

References

[1] Kumar N, Sun Y, Xu N, Manna K, Yao M, Süss V, Leermakers I, Young O, Förster T, Schmidt M, Borrmann H, Yan B, Zeitler U, Shi M, Felser C and Shekhar C 2017 *Nat. Commun.* **8** 1642
[2] Wang A, Graf D, Liu Y, Du Q, Zheng J, Lei H and Petrovic C 2017 *Phys. Rev. B* **96** 121107
[3] Lv Y Y, Li X, Zhang J, Pang B, Chen S S, Cao L, Zhang B B, Lin D, Chen Y B, Yao S H, Zhou J, Zhang S T, Lu M H, Tian M and Chen Y F 2018 *Phys. Rev. B* **97** 245151
[4] Razzoli E, Zwartsenberg B, Michiardi M, Boschini F, Day R P, Elfimov I S, Denlinger J D, Süss V, Felser C and Damascelli A 2018 *Phys. Rev. B* **97** 201103
[5] Liu X, Yu Z, Li J, Xu Z, Zhou C, Dong Z, Zhang L, Wang X, Yu N, Zou Z, Wang X and Guo Y 2023 *Chin. Phys. B* **32** 018102
[6] Wang Y Y, Yu Q H, Guo P J, Liu K and Xia T L 2016 *Phys. Rev. B* **94** 041103
[7] Yuan Z, Lu H, Liu Y, Wang J and Jia S 2016 *Phys. Rev. B* **93** 184405
[8] Shen B, Deng X, Kotliar G and Ni N 2016 *Phys. Rev. B* **93** 195119

[9] Takahashi H, Okazaki R, Ishiwata S, Taniguchi H, Okutani A, Hagiwara M and Terasaki I 2016 *Nat. Commun.* **7** 12732
[10] Bentien A, Johnsen S, Madsen G K H, Iversen B B and Steglich F 2007 *Europhys. Lett.* **80** 17008
[11] Du Q, Guzman D, Choi S and Petrovic C 2020 *Phys. Rev. B* **101** 035125
[12] Sun P, Oeschler N, Johnsen S, Iversen B B and Steglich F 2009 *Appl. Phys. Express* **2** 091102
[13] Gippius A A, Baenitz M, Okhotnikov K S, Johnsen S, Iversen B and Shevelkov A V 2014 *Appl. Magn. Reson.* **45** 1237
[14] Zhang L, Wang Y and Chang H 2020 *Materials* **13** 3159
[15] Petrovic C, Lee Y, Vogt T, Lazarov N, Bud'ko S and Canfield P 2005 *Phys. Rev. B* **72** 045103
[16] Zhu J, Ren Q, Chen C, Wang C, Shu M, He M, Zhang C, Le M D, Torri S, Wang C-W, Wang J, Cheng Z, Li L, Wang G, Jiang Y, Wu M, Qu Z, Tong X, Chen Y, Zhang Q and Ma J 2024 *Nat. Commun.* **15** 2618
[17] Vasiliev A N, Voloshok T N, Granato A V, Joncich D M, Mitrofanov Y P and Khonik V A 2009 *Phys. Rev. B* **80** 172102
[18] Nakamura K, Takahashi Y and Fujiwara T 2014 *Sci. Rep.* **4** 6523
[19] Delaire O, May A F, McGuire M A, Porter W D, Lucas M S, Stone M B, Abernathy D L, Ravi V A, Firdosy S A and Snyder G J 2009 *Phys. Rev. B* **80** 184302
[20] Wu J, Lin Y, Shu M, Liu Y, Ma Y, Lin G, Zhang C, Jiao P, Zhu F, Wu Y, Ewings R A, Walker H C, Deng G, Chi S, Jiang S, Baggioli M, Jin M, Wang H, Xie W, Wei T R, Yang J, Shi X and Ma J 2024 *Nat. Commun.* **15** 6248
[21] Krivchikov A I, Vdovichenko G A, Korolyuk O A, Bermejo F J, Pardo L C, Tamarit J L, Jezowski A and Szewczyk D 2015 *J. Non. Cryst. Solids* **407** 141
[22] Baran A, Botko M, Kajňaková M, Feher A, Feodosyev S, Syrkin E, Klochko M, Tovstyuk N, Grygorchak I and Fomenko V 2015 *Low Temp. Phys.* **41** 930
[23] Baggioli M and Zaccone A 2019 *J. Phys.: Mater.* **3** 015004
[24] Krivchikov A I, Jeżowski A, Szewczyk D, Korolyuk O A, Romantsova O O, Buravtseva L M, Cazorla C and Tamarit J L 2022 *J. Phys. Chem. Lett.* **13** 5061
[25] Cano A and Levanyuk A P 2004 *Phys. Rev. B* **70** 212301
[26] Du Q, Tong X, Liu Y and Petrovic C 2021 *Appl. Phys. Lett.* **118** 171904
[27] Lazarević N, Popović Z V, Hu R and Petrovic C 2010 *Phys. Rev. B* **81** 144302
[28] Lin G T, Wang Y Q, Luo X, Ma J, Zhuang H L, Qian D, Yin L H, Chen F C, Yan J, Zhang R R, Zhang S L, Tong W, Song W H, Tong P, Zhu X B and Sun Y P 2018 *Phys. Rev. B* **97** 064405
[29] Wan Y, Jiao J, Lin G, Wu Y, Wang X, Zhang R, Sun Q, Tong W, Wang G, Ren Q, Zhu J, Zhao B, Zhang M, Chen M, Weissenrieder J, Yao X and Ma J 2023 *J. Alloys Compd.* **932** 167526
[30] Jin F, Ma X, Guo P, Yi C, Wang L, Wang Y, Yu Q, Sheng J, Zhang A, Ji J, Tian Y, Liu K, Shi Y, Xia T and Zhang Q 2016 *Phys. Rev. B* **94** 094302
[31] Racu A M, Menzel D, Schoenes J, Marutzky M, Johnsen S and Iversen B B 2008 *J. Appl. Phys.* **103** 07C912
[32] Racu A M, Menzel D, Schoenes J and Doll K 2007 *Phys. Rev. B* **76** 115103
[33] Acharyya P, Ghosh T, Pal K, Rana K S, Dutta M, Swain D, Etter M, Soni A, Waghmare U V and Biswas K 2022 *Nat. Commun.* **13** 5053
[34] Lazarević N, Radonjić M M, Tanasković D, Hu R, Petrovic C and Popović Z V 2012 *J. Phys.: Condens. Matter* **24** 255402
[35] Fuccillo M K, Gibson Q D, Ali M N, Schoop L M and Cava R J 2013 *APL Materials* **1** 062102
[36] Xu W, Lin G, Shu M, Jiao J, Zhu J, Ren Q, Le M D, Luo X, Sun Y, Liu Y, Qu Z, Zhou H, Gao S and Ma J 2024 *Chin. Phys. Lett.* **41** 117503
[37] Kresse G and Furthmüller J 1996 *Phys. Rev. B* **54** 11169
[38] Kresse G and Furthmüller J 1996 *Comput. Mater. Sci* **6** 15
[39] Kresse G and Joubert D 1998 *Phys. Rev. B* **59** 3
[40] Furness J W, Kaplan A D, Ning J, Perdew J P and Sun J 2020 *J. Phys. Chem. Lett.* **11** 8208
[41] Togo A and Tanaka I 2015 *Scr. Mater.* **108** 1
[42] Togo A 2001 *J. Phys. Soc. Jpn.* **92** 012001